ADVANCED FUNCTIONAL MATERIALS
www.afm-journal.de

Designing Head-to-Tail Topological Vinylene-Bridged Dimer Acceptor for Efficient and Stable Organic Solar Cells

Wendi Shi, Qiansai Han, Wenkai Zhao, Zheng Xu, Ziqi Ma, Ruohan Wang, Guankui Long, Zhaoyang Yao, Chenxi Li, Xiangjian Wan, and Yongsheng Chen**

Dimerized small-molecule acceptors are promising materials for high-performance organic solar cells (OSCs), yet the diversity of their topological configurations remains underexplored. In this study, two dimer acceptors are designed and investigated, QD-2 and QD-3, constructed via an unconventional "head-to-tail" linkage of Y-series building blocks, bridged by vinylene and ethynylene units, respectively. Comprehensive characterization reveals that QD-2 simultaneously suppresses energy disorder and electron–phonon coupling while facilitating favorable molecular stacking. These features yield a fibrous film morphology with improved exciton and charge dynamics. As a result, QD-2-based OSCs achieve outstanding power conversion efficiencies (PCEs) of 19.39% in binary and 20.04% in ternary devices, surpassing the QD-3-based binary counterpart (18.05%). Moreover, both QD-2 and QD-3 exhibit high glass transition temperatures (Tg), conferring excellent thermal stability to their devices. This work highlights the critical role of linker chemistry and molecular topology in advancing dimer acceptor design and offers a guiding framework for next-generation OSC materials.

1. Introduction

In recent years, OSCs have experienced rapid development, with the PCE of single-junction OSCs achieving over 20%.[1–6] This significant advancement primarily stems from the persistent development of organic photoactive materials, with a pivotal contribution coming from the emergence of non-fullerene small-molecule acceptors (SMAs), notably the Y6 family and its structural derivatives.[7–12] Nevertheless, conventional SMAs exhibit inherent limitations including depressed Tg and elevated diffusion coefficients. These characteristics promote excessive molecular diffusion, leading to gradual deterioration of the bulk heterojunction (BHJ) morphological stability.[13,14] To address this issue, molecular oligomerization strategies for constructing giant molecule acceptors (GMAs) have emerged as a promising approach to regulate active layer morphology while simultaneously enhancing optoelectronic performance and device stability.[15,16] In contrast to conventional SMAs and polymer acceptors (PAs), GMAs possess precisely defined molecular structures, increased molecular dimensions, and elevated Tg. Furthermore, GMAs circumvent two critical limitations of all-polymeric systems: the batch-dependent performance variations inherent to PAs and the morphological constraints imposed by polymer chain entanglements in all-polymer blends.[17]

Among various GMAs, dimer acceptors have attracted the most extensive research attention. The optoelectronic properties of these dimers are critically determined by three design parameters: 1) the composition of monomer units, 2) the chemical structure of the linking moiety, and 3) the specific connection sites, all of which collectively govern molecular conformation and solid-state packing behavior. Currently, high-performance dimer acceptors primarily incorporate Y-series derivatives as building blocks, with the majority adopting one of four conventional linking modes to connect two identical SMA units: tail-to-tail,[18–20] head-to-head,[21–23] inner-side chain,[24,25] or outer-side chain[26,27] configurations (**Figure 1a**). While these approaches have achieved substantial success, their limited structural diversity restricts further optimization of key photovoltaic parameters. Notably, most high-efficiency dimerized acceptors reported to date utilize flexible linkers, which inevitably introduce conformational disorder.[25,28] In contrast, rigid π-bridged linkers can construct a more constrained backbone and facilitate coplanar conformations, promoting ordered molecular packing and reducing disorder, thereby enhancing charge transport.[29,30]

Recently, our group has developed a series of high-performance acceptors with center core extension conjugation,

W. Shi, Q. Han, Z. Xu, Z. Ma, R. Wang, Z. Yao, C. Li, X. Wan, Y. Chen
State Key Laboratory of Elemento-Organic Chemistry
Frontiers Science Center for New Organic Matter
Key Laboratory of Functional Polymer Materials
Institute of Polymer Chemistry
Tianjin Key Laboratory of functional polymer materials
Nankai University
Tianjin 300071, China
E-mail: xjwan@nankai.edu.cn; yschen99@nankai.edu.cn
W. Zhao, G. Long
School of Materials Science and Engineering
National Institute for Advanced Materials
Nankai University
Tianjin 300350, China

The ORCID identification number(s) for the author(s) of this article can be found under https://doi.org/10.1002/adfm.202523116

DOI: 10.1002/adfm.202523116

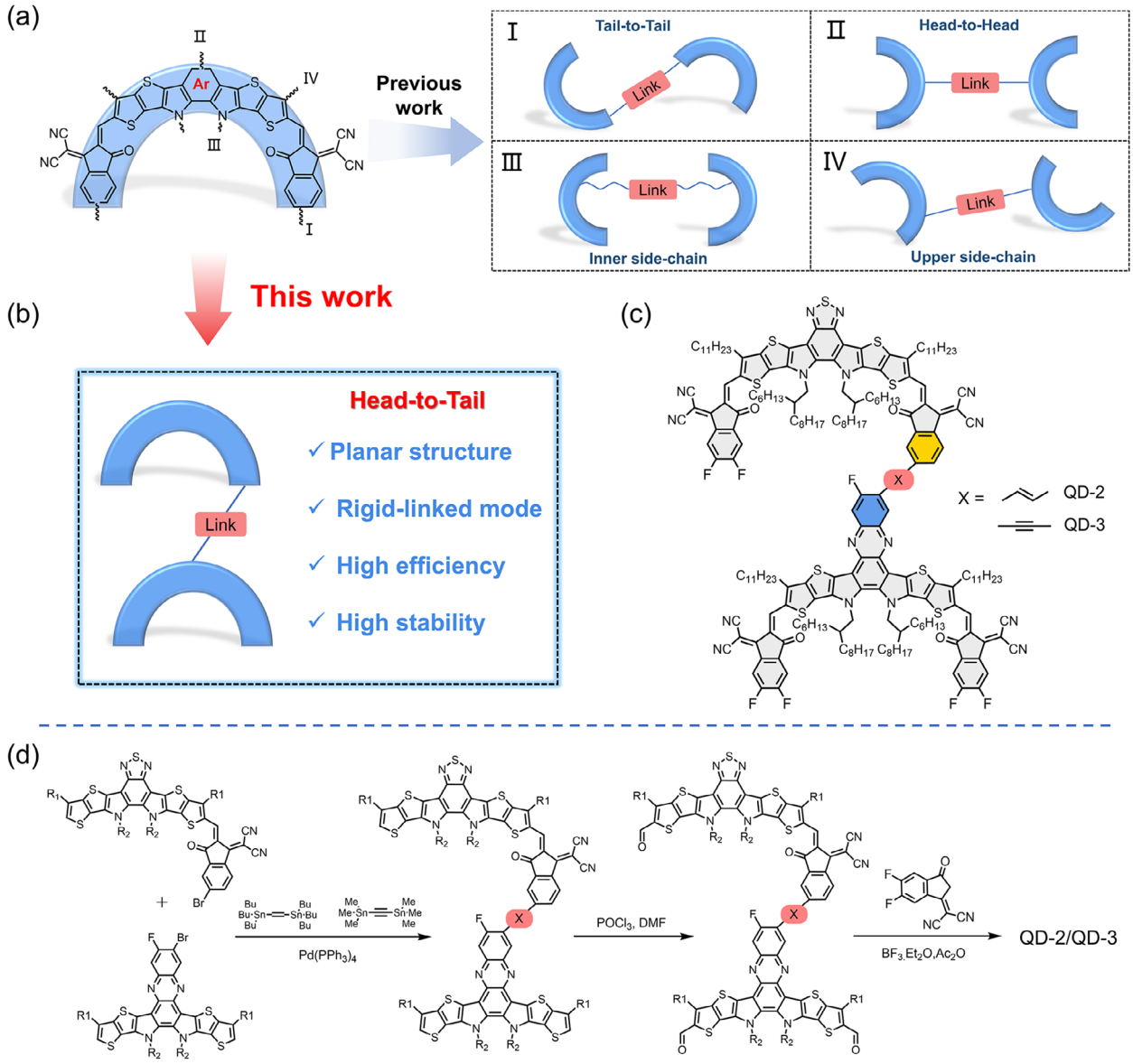

Figure 1. Linking modes for the dimer acceptors a) in previous work and b) in this work. c) Molecular structures of QD-2 and QD-3. d) Synthetic routes of QD-2 and QD-3.

in which the two-dimensionally conjugated central core provides additional modification sites, offering new possibilities for dimerization at the central core (as demonstrated in head-to-head dimers).[11,22] Moreover, these acceptors have exhibited reduced reorganization energy due to their more rigid backbone, as well as enhanced ordered packing, which promotes charge transport and suppresses charge recombination. The topological configuration of dimer acceptors plays a critical role in determining molecular packing, film morphology, and ultimately device performance. Vinylene (—CH═CH—) and ethynylene (—C≡C—) are non-aromatic unsaturated groups with minimal steric hindrance due to their lack of ring structures, making them effective linkers for achieving planar conformations. Previous studies have confirmed that vinylene/ethynylene-bridged GMA (in tail-to-tail or head-to-head configurations) exhibit reduced backbone torsion.[31,32] Building upon this structure-property understanding, we employed these rigid linkers to design the head-to-tail dimer acceptors QD-2 and QD-3 (Figure 1b,c), with the specific aim of enforcing a planar conformation and enhancing molecular packing. Unlike conventional dimers acceptors, these novel topological dimer acceptors achieve the following innovations: 1) Breaking through traditional connection site limitations, a head-to-tail specific coupling was achieved by linking the end group and central core of the Y-series monomer, constructing a unique "2"-shaped topological dimerized acceptor. 2) A systematic investigation revealed the structure-property relationships between different linkers (vinylene vs ethynylene) and the photophysical properties, thin-film morphology, and device performance of head-to-tail dimers. Experimental results demonstrated that QD-2 achieved 19.39% binary and 20.04%

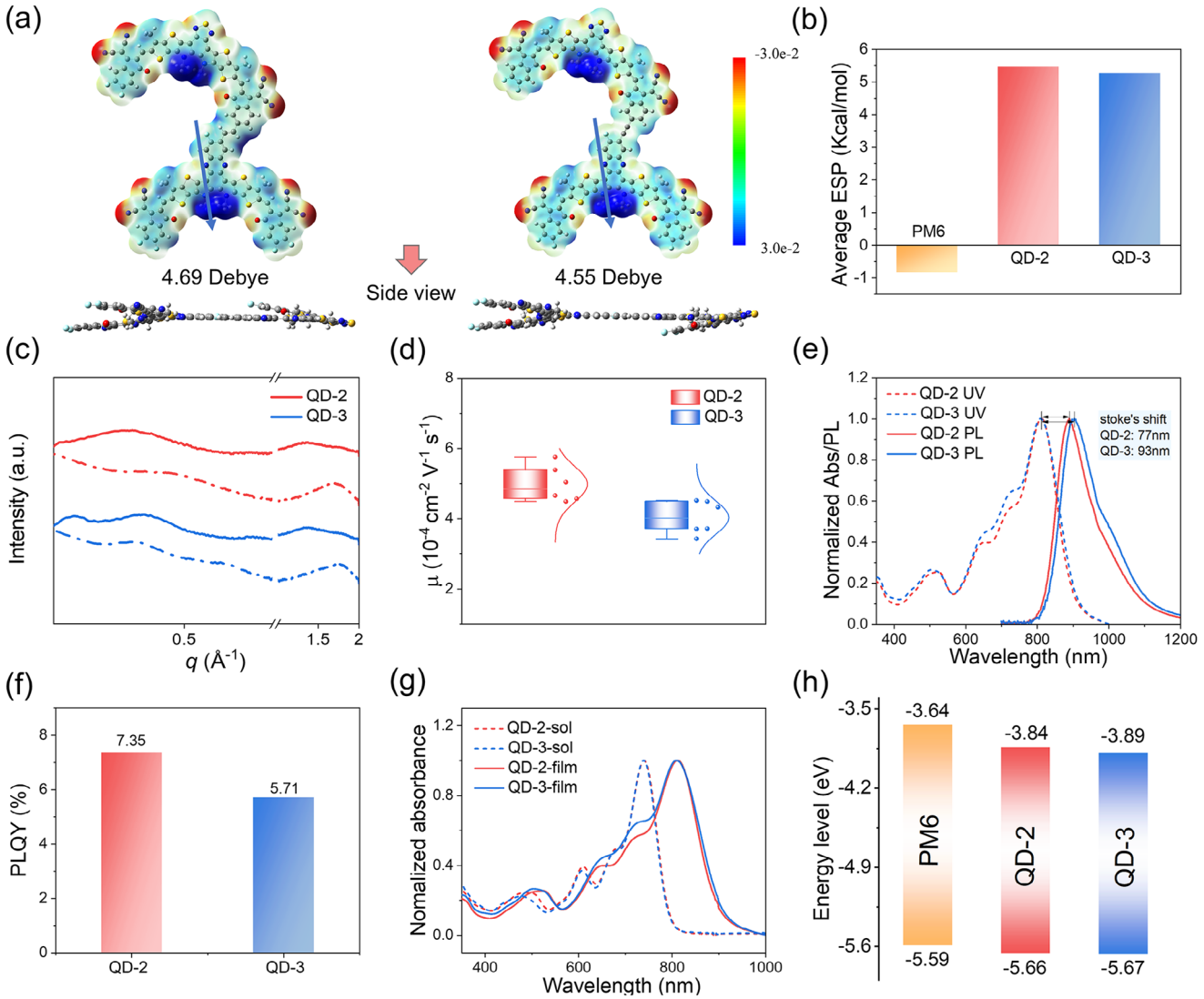

Figure 2. a) The electrostatic surface potential maps and side views of QD-2 and QD-3, optimized at the B3LYP/6-31G level of DFT calculations. b) Average ESP values of PM6, QD-2, and QD-3. c) GIWAXS in-plane (solid lines) and out-of-plane (dotted lines) line-cut profiles of the pristine dimer films. d) The statistical chart of electron mobilities of QD-2 and QD-3 pristine film. e) UV–vis absorption (abs.) and photoluminescence (PL) spectra of QD-2 and QD-3 in the films. f) PLQY of QD-2 and QD-3 in flim. g) Normalized absorption spectra of QD-2 and QD-3 in the $CHCl_3$ solution and in the films. h) Energy levels of PM6, QD-2 and QD-3.

ternary (as host acceptor) PCEs, attributed to its low energy disorder, order molecular stacking, and ideal phase separation. In contrast, QD-3 exhibited excessive intermolecular aggregation, leading to a lower PCE of 18.05%. Notably, both of these dimer acceptors exhibited excellent thermal stability. This work not only provides a feasible strategy for constructing new topological dimer acceptors but also highlights the critical role of linker-molecular configuration synergy by elucidating the strong correlation between molecular conformation, morphological characteristics, and photovoltaic performance.

2. Results and Discussion

The dimer acceptors QD-2 and QD-3 were synthesized via palladium-catalyzed Stille cross-coupling (Figure 1d; Schemes S1–S6, Supporting Information). The detailed synthesis steps are described in the supporting information. Both molecules exhibit high thermal stability, as evidenced by decomposition temperatures (Td) of 336 °C for QD-2 and 341 °C for QD-3 (Figure S1, Supporting Information). Density functional theory (DFT) calculations were performed to analyze their molecular geometries and electronic properties. As illustrated in **Figure 2a** and S2 (Supporting Information), both molecules adopt a planar conformation resembling the numeral "2". This unique asymmetric geometry endows them with large dipole moments (4.69 D for QD-2; 4.55 D for QD-3), which is beneficial to promote intermolecular interactions and facilitate molecular packing. The results of the surface electrostatic potential (ESP) have demonstrated the affinity characteristics of the two acceptors but due to the slightly enhanced electron-donating

property of the vinylene unit, QD-2 exhibits a higher average ESP (5.46 kcal mol^{-1}) than QD-3 (5.28 kcal mol^{-1}) (Figure S3, Supporting Information). As a result, the increased average ESP value of QD-2 effectively enlarges the ESP margin with PM6 (Figure 2b), thus enhancing their interfacial interaction.

Grazing incidence wide-angle X-ray scattering (GIWAXs) of the pure films was used to reveal the molecular ordered packing. As shown in Figure 2c and Figure S4, Table S1 (Supporting Information), QD-2 displays face-on orientation, evidenced by the (010) peak in the out-of-plane (OOP) direction and (100) peak in the in-plane (IP) direction. Though QD-3 also demonstrates face-on molecular orientation, the presence of a strong IP diffraction peak at 0.23 $Å^{-1}$ in QD-3 indicates its orientational stacking is less ordered than that of QD-2. Notably, QD-3 exhibits tighter π–π stacking and a longer crystal coherence length (CCL) than QD-2, likely due to the more rigid linear structure of the ethynylene, which eliminates rotational freedom and thus forms a more planar skeletal structure. Surprisingly, despite its tighter packing, QD-3 shows lower electron mobility than QD-2 (Figure 2d). We hypothesize that excessive molecular aggregation in QD-3 strengthens vibrational coupling, which impairs charge transport. To test this, we measured the Stokes shift of neat films. As shown in Figure 2e, QD-2 exhibits a smaller Stokes shift (77 vs 93 nm for QD-3), suggesting low reorganization energy. Further analysis of the Huang–Rhys parameter (S) confirms weaker electron-phonon coupling in QD-2 (Table S2, Supporting Information), consistent with its higher electron mobility.[33–35] As displayed in Figure 2f and Figure S5 (Supporting Information), this reduced coupling also suppresses non-radiative losses, yielding a higher photoluminescence quantum yield (PLQY) for QD-2 (7.35% vs 5.71% for QD-3).

As shown in Figure 2g, the two dimer acceptors in solution exhibit nearly identical absorption ranges, with maximum absorption peaks located at 740 nm. The absorption spectra of the pure films for QD-2 and QD-3 exhibit a redshift relative to their spectra in solution, which is attributed to molecular aggregation. The 0-0 absorption peaks are located at 813 nm for QD-2 and 811 nm for QD-3. It is worth noting that, compared to QD-2, the 0-1 absorption peak of QD-3 is more pronounced. Therefore, an enhanced intensity ratio of 0-0 to 0-1 absorption can be observed for QD-2 films compared to QD-3 films, implying enhanced *J*-aggregation character in QD-2.[36–38] Furthermore, relative to QD-3, QD-2 showed a sharper absorption onset in the thin film, which indicated that the Urbach Energy (E_U) of the QD-2 film was smaller than that of QD-3.[39] We applied Fourier transform photocurrent spectroscopy external quantum efficiency (FTPS-EQE) to quantificationally investigate the E_U in the QD-2 and QD-3 neat films. As shown in Figure S6 (Supporting Information), the QD-2 neat film exhibits a low energy disorder with an *E*u of 20.9 meV, which is smaller than that of the QD-3 electron acceptor (22.5 meV). The trends of the theoretical highest occupied molecular orbital (HOMO) and lowest unoccupied molecular orbital (LUMO) levels of QD-2 and QD-3 are consistent with the results obtained by cyclic voltammetry (CV), as shown in Figures S7 and S8 (Supporting Information) and Figure 2h. The downshifted HOMO and LUMO levels in QD-3 vs QD-2 arise from the stronger electron-withdrawing effect of its sp-hybridized acetylene linker.

To investigate the correlation between molecular structure and device performance, we selected PM6 as the polymer donor due to its complementary absorption and well-matched energy levels with the two acceptors, and fabricated conventional ITO/2PACz/Active Layer/PNDIT-F3N/Ag devices. The current density-voltage (*J*–*V*) curves of the optimal devices based on QD-2 and QD-3 are shown in **Figure 3a**, and the detailed photovoltaic performance parameters are summarized in **Table 1**. The optimal PCE values for PM6:QD-2 and PM6:QD-3-based binary OSCs are 19.39% and 18.05%, respectively. The PM6:QD-2 binary OSCs exhibited a higher J_{SC} of 26.95 mA cm^{-2} compared to 26.58 mA cm^{-2} for PM6:QD-3, which is attributed to the PM6:QD-2 system's superior charge generation, consistent with its enhanced EQE response across the 450 to 800 nm region (Figure 3b). The higher V_{OC} of 0.900 V in PM6:QD-2 compared to 0.877 V in PM6:QD-3 results from QD-2′s higher-lying LUMO energy level and lower energy disorder. Furthermore, the PM6:QD-3 device exhibited a lower FF (77.41%) compared to PM6:QD-2 (79.95%), which we attribute to excessive aggregation of QD-3. A more in-depth morphological analysis will be discussed in the following section. To further improve the device efficiency, we fabricated an optimized ternary system by incorporating 25 wt.% BO-4Cl, a narrow-bandgap acceptor with extended near-infrared absorption. The ternary device achieved a champion PCE of 20.04% with a V_{OC} of 0.894 V, J_{SC} of 28.15 mA cm^{-2}, and FF of 79.62%. It is noteworthy that this PCE is one of the highest values reported for dimer-acceptor-based OSCs to date (Table S3, Supporting Information). Furthermore, statistical analysis of 15 independent devices confirmed excellent reproducibility (Figure 3c; Tables S4–S6, Supporting Information).

To understand the fundamental mechanisms underlying the pronounced performance differences, we systematically investigated the exciton dissociation dynamics and charge transport behavior in these photovoltaic devices. Space-charge-limited current (SCLC) measurements of electron-only and hole-only devices (Figure 3d; Figure S9, Supporting Information) revealed that all devices exhibited higher hole mobility (μ_h) than electron mobility (μ_e). Notably, the ternary device demonstrated significantly improved carrier mobility. The μ_h/μ_e of PM6:QD-2, PM6:QD-3, and PM6:QD-2:BO-4Cl are 1.10, 1.31, and 1.11, respectively, which correlates well with the observed FF variations. The particularly unbalanced charge transport in PM6:QD-3 devices would lead to bimolecular and trap-assisted recombination during the carrier transport, as confirmed by light intensity-dependent of V_{OC} and J_{SC} measurements (Figures S10 and S11, Supporting Information). In the plot of light intensity versus *V*oc, the slope is closer to kT/q, suggesting that trap-assisted recombination is suppressed. The slopes for the PM6:QD-2, PM6:QD-3 and PM6:QD-2:BO-4Cl-based devices are 1.25 KT/q, 1.44 KT/q and 1.20 KT/q, respectively. Comparative analysis demonstrates that trap-assisted recombination is significantly suppressed in the ternary device, whereas it remains dominant in the PM6:QD-3 system. Similarly, in the plot of light intensity versus J_{SC}, the QD-2-based binary and ternary devices exhibit an exponential factor of 0.998, which is closer to 1 than the QD-3 base device (0.996), indicating reduced bimolecular recombination.

We analyzed the photocurrent density (J_{ph}) versus effective voltage (V_{eff}) characteristics to quantify exciton dissociation (P_{diss}) and charge collection efficiencies (P_{coll}). The P_{diss} was determined from the J_{ph}/J_{sat} ratio at short-circuit conditions, where J_{ph} is the photocurrent density and J_{sat} represents the saturation

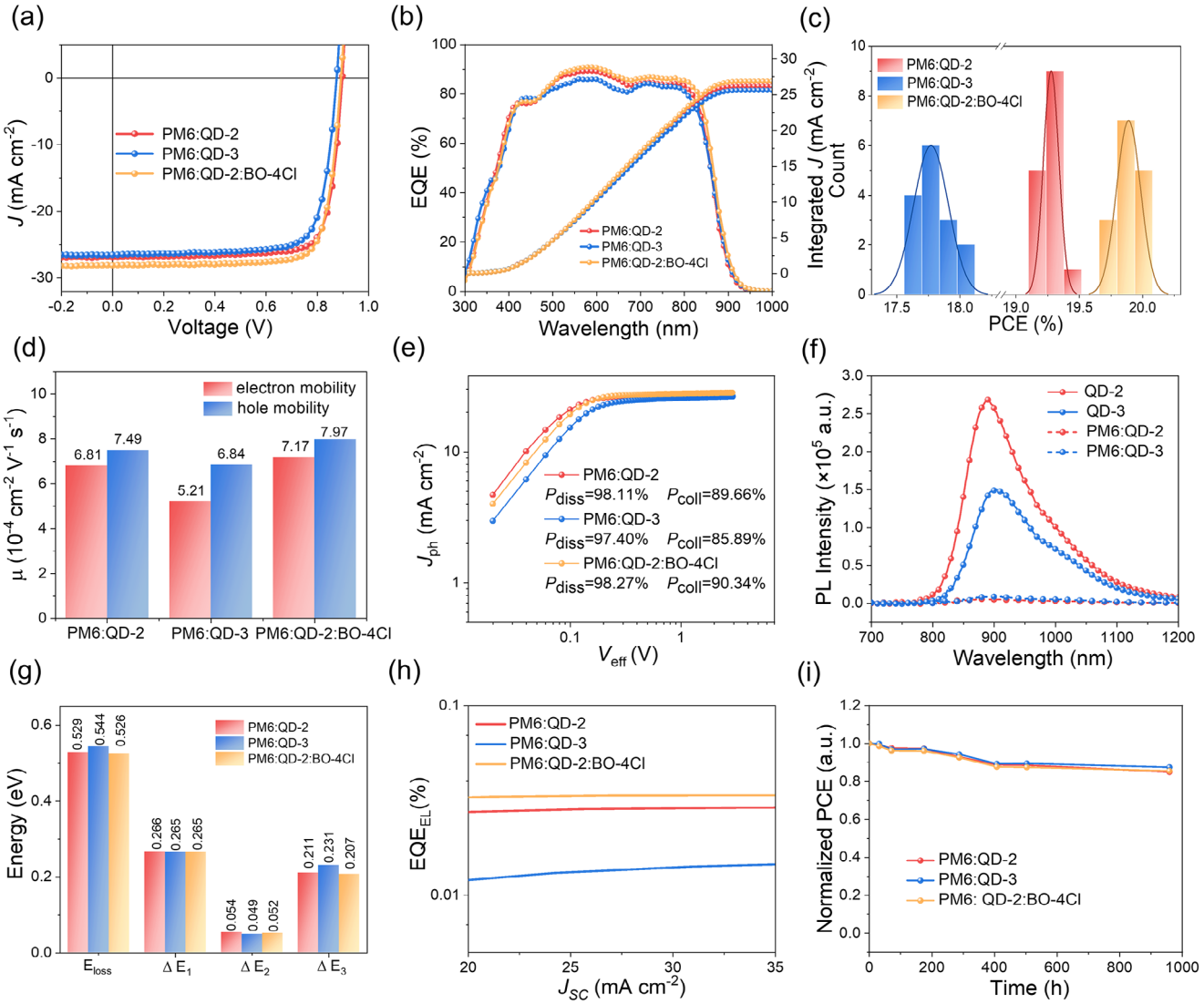

Figure 3. a) *J–V* curves for OSCs. b) EQE plots and integrated J_{SC} curves. c) Statistical histograms of PCEs of OSCs based on PM6: QD-2, PM6: QD-3, and PM6: QD-2: BO-4Cl. d) The electron and hole mobilities of the PM6: QD-2, PM6: QD-3, and PM6: QD-2: BO-4Cl blends acquired from single-carrier devices. e) J_{ph} versus V_{eff} curves indicating P_{diss} and P_{coll}. f) Photoluminescence spectra of neat and blend films. g) Summary of detailed energy losses terms of optimal devices h) the corresponding EQE_{EL} spectra for optimized OSCs. i) thermal stability of PM6:QD-2, PM6: QD-3 and PM6:QD-2: BO-4Cl based OSCs without encapsulation in a nitrogen-filled glove box at 65 °C.

photocurrent density. Correspondingly, the P_{coll} was derived from the J_{ph}/J_{sat} ratio at the maximum power point. As shown in Figure 3e, the PM6:QD-2, PM6:QD-3, and PM6:QD-2:BO-4Cl devices exhibited P_{diss}/P_{coll} values of 98.11%/89.66%, 97.40%/85.89%, and 98.27%/90.34%, respectively. The enhanced P_{diss} and P_{coll} values in the ternary systems suggest more efficient exciton dissociation and charge transport processes, which is attributed to its more ideal morphology of the active layer. Additionally, the enhanced P_{diss} in PM6:QD-2 device is further corroborated by photoluminescence quenching measurements, showing a significantly higher quenching yield of 98% compared to 94% for PM6:QD-3 blends (Figure 3f).

We performed transient photocurrent (TPC) and transient photovoltage (TPV) measurements to evaluate charge extraction dynamics and photogenerated carrier lifetimes in QD-2 and QD-3-based devices. The TPC results (Figure S12, Supporting Information) demonstrate that the QD-2-based ternary OSC exhibits significantly shorter charge extraction time (τ = 0.40 μs) compared to the QD-3 device (τ= 0.53 μs), indicating more efficient charge generation and collection with fewer charge traps. Furthermore, TPV measurements reveal an extended carrier lifetime ($\tau_{binary}/\tau_{ternary}$ = 35/36 μs) in QD-2-based OSCs versus 16 μs for QD-3 devices (Figure S13, Supporting Information), consistent with suppressed recombination in the QD-2 system.

To elucidate the origin of the V_{OC} differences between QD-2 and QD-3 systems, we systematically analyzed the energy loss (E_{loss}) mechanisms in these photovoltaic devices (Figure 3g; Table S7, Supporting Information). Based on the Shockley-Queisser (SQ) limit theory, the E_{loss} can be divided into three distinct components: $E_{loss} = \Delta E_1 + \Delta E_2 + \Delta E_3$. The bandgap energies,

Table 1. Photovoltaic performance parameters of OSCs based on PM6:QD-2, PM6:QD-3 and PM6:QD-2:BO-4Cl and measured under the illumination of AM 1.5G (100 mW cm^{-2}).

Active layers	V_{OC} [V]	J_{SC} [mA cm^{-2}]	J_{SC}^{EQE}[mA cm^{-2}]	FF [%]	PCE [%] [a]
PM6: QD-2	0.900(0.897±0.003)	26.95(27.14±0.20)	26.18	79.95(79.22±0.49)	19.39(19.28±0.06)
PM6: QD-3	0.877(0.873±0.007)	26.58(26.55±0.35)	25.61	77.41(76.71±0.78)	18.05(17.77±0.14)
PM6: QD-2:BO-4Cl	0.894(0.892±0.003)	28.15(28.13±0.15)	26.88	79.62(79.27±0.33)	20.04(19.89±0.10)

[a] The average values in parentheses were obtained from 15 independent devices.

determined from differentiating the EQE spectra (dEQE/dE) (Figure S14, Supporting Information), were 1.429, 1.422 and 1.420 eV for PM6:QD-2, PM6:QD-3, and PM6:QD-2:BO-4Cl blends, respectively. Corresponding total energy losses measured 0.529, 0.545, and 0.526 eV, revealing QD-2 systems' advantage in voltage preservation. The radiative loss above the bandgap (ΔE_1) is unavoidable for all types of solar cells determined only by the bandgap. The below-bandgap radiative losses (ΔE_2) exhibited negligible differences (0.049–0.054 eV) among all devices. However, the non-radiative loss (ΔE_3) demonstrated marked differences. Through electroluminescence quantum efficiency (EQE_{EL}) measurements (Figure 3h), we found that both binary and ternary QD-2-based devices exhibited superior EQE_{EL} values (2.8×10^{-4} and 3.3×10^{-4}) compared to QD-3 (2.1×10^{-4}), with corresponding ΔE_3 values (0.211, 0.207 eV) substantially lower than the 0.231 eV observed in QD-3 devices, which is also consistent with the higher PLQY of QD-2.

To better understand nonradiative energy losses, we calculated the E_U of blend films as a quantitative measure of energy disorder, which closely correlates with nonradiative recombination. As shown in Figure S15 (Supporting Information), the *E*u was obtained by fitting the low photon energy region from the FTPS-EQE spectrum. The Eu values for PM6:QD-2, PM6:QD-3, and PM6:QD-2:BO-4Cl are 20.6, 21.7, and 20.6 meV, respectively. The lower E_U values in QD-2-based devices indicate reduced energy disorder, consistent with their suppressed nonradiative recombination. This enhancement stems from improved molecular ordering in the QD-2 blend films, as will be discussed below.

The morphological stability of OSCs is critically influenced by the diffusion coefficients of acceptors, which can be indirectly characterized through Tg.[40] We estimated Tg values by monitoring UV–vis absorbance changes in thin films during thermal annealing (40–170 °C). As shown in Figure S16 (Supporting Information), both QD-2 (Tg = 90 °C) and QD-3 (Tg = 87 °C) exhibit significantly elevated transition temperatures compared to BO-4Cl (Tg = 69 °C), primarily due to their large molar masses as dimer acceptors.[13] These high Tg values effectively suppress molecular diffusion in blend films, thereby enhancing morphological stability. Consistent with this understanding, the PM6:QD-2, PM6:QD-3, and PM6:QD-2:BO-4Cl blends exhibited excellent thermal stability, maintaining 85%, 87%, and 85% of their original PCE after 960-h aging at 65 °C (Figure 3i). This level of stability significantly surpasses that of the PM6:BO-4Cl binary blend (Figure S17, Supporting Information), thereby directly validating our initial design strategy of developing dimerized acceptors for improved device durability.

Transient absorption spectroscopy (TAS) was employed to investigate exciton dynamics and charge transport processes. We selected an 800 nm low-power pump light to specifically excite acceptor molecules. As shown in **Figure** 4a and S18 (Supporting Information), the immediate appearance of a ground state bleach (GSB) signal at 630 nm (corresponding to PM6 absorption) following selective acceptor excitation indicates rapid hole transfer from acceptor to donor molecules.

The donor GSB signal kinetic data at 630 nm were analyzed using biexponential fitting to track the hole transfer dynamics (Figure 4b,c). The kinetic analysis reveals two distinct charge generation processes: the rapid component (τ_1) reflects exciton separation at donor-acceptor interfaces, whereas the slow component (τ_2) characterizes the exciton diffusion process towards interfaces before dissociation.[41] Among the studied systems, the ternary PM6:QD-2:BO-4Cl composite shows optimal time constants (τ_1 = 0.31 ps; τ_2 = 4.23 ps), indicating enhanced excitonseparation efficiency and improved charge carrier transport compared to binary blends (PM6:QD-2: τ_1 = 0.42 ps, τ_2 = 7.64 ps; PM6:QD-3: τ_1 = 0.62 ps, τ_2 = 12.97 ps). This accelerated charge generation mechanism directly correlates with the observed improvements in photovoltaic performance parameters.

To elucidate the intermolecular interaction mechanisms and packing morphology between donor and acceptor materials at the molecular level in PM6:QD-2 and PM6:QD-3 systems, we systematically investigated the spatial arrangement of each component using molecular dynamics (MD) simulations (**Figure** 5a).[42,43] As displayed in Figure S19 (Supporting Information), PM6 is divided into two distinct segments (designated C and E) and QD-2/QD-3 acceptor molecules are segmented into three distinct segments (labeled A, D, and A'). Through this segmentation approach, six possible molecular packing conditions were characterized. Then, the intermolecular packing behavior was analyzed through computation of radial distribution functions (RDFs) between PM6 and the acceptor molecules, as presented in Figure S20 (Supporting Information). All blend systems exhibited pronounced peaks at 3.8–4.0 Å in the RDF profiles, which correlate well with the π–π stacking distances determined by GIWAXS analysis. Notably, under CA' and EA' packing conditions, the RDF of QD-2 exhibits a significantly sharper peak at π–π stacking distances compared to QD-3, indicating enhanced molecular ordering in the stacking arrangement. However, the analysis of stacking densities reveals that both total stacking counts and face-on oriented stacking counts per unit volume were higher in the PM6:QD-3 system compared to PM6:QD-2 (Table S8 and Figure S9, Supporting Information). The enhanced molecular packing orderliness observed in QD-2 is accompanied by a concomitant decrease in stacking numbers, suggesting a trade-off between structural regularity

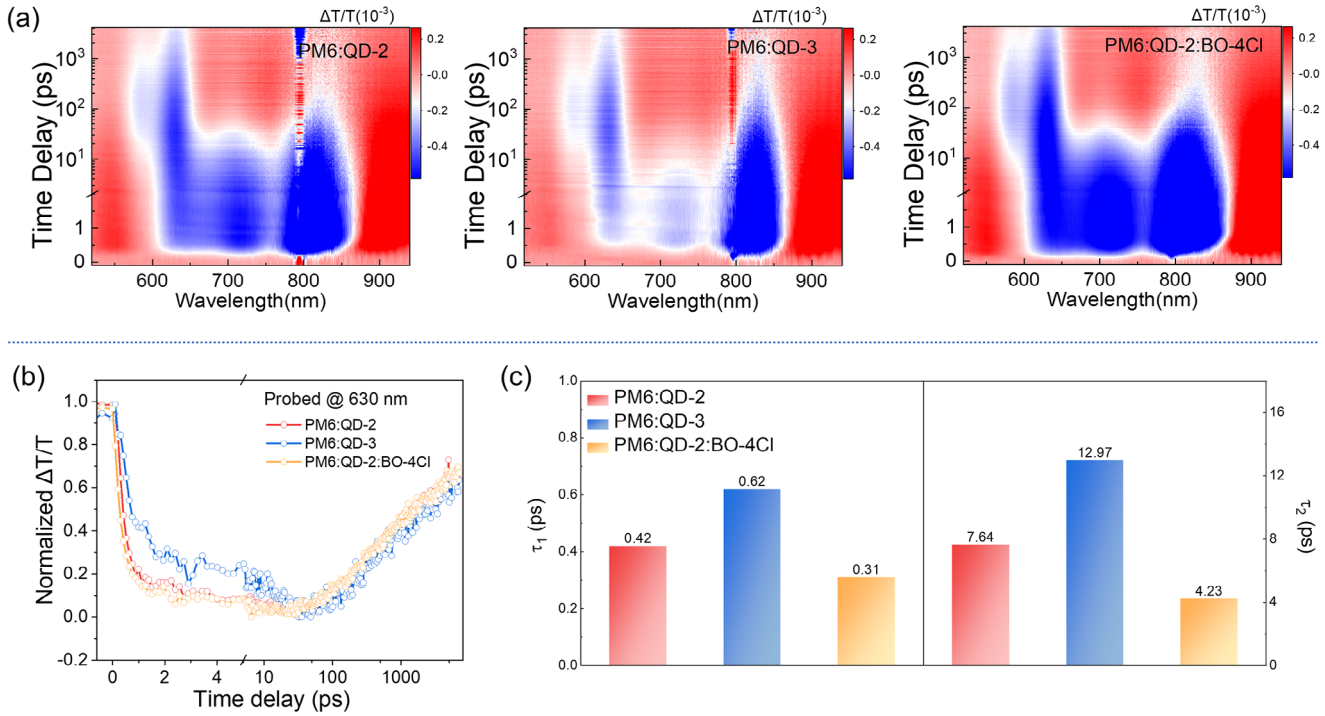

Figure 4. TA result of PM6:QD-2, PM6:QD-3 and PM6:QD-2:BO-4Cl blend films. (a) Contour plots of the time-resolved absorption difference spectra of the blend films under 800 nm excitation. b) The hole transfer process at 630 nm. c) Statistical graphs of charge-transfer time and lifetime achieved through multi-exponential fitting in corresponding conditions.

and intermolecular interactions. Furthermore, MD simulations were also conducted on the PM6:QD-2:BO-4Cl ternary system to investigate the impact of BO-4Cl addition on system packing. Stacking numbers revealed that the ternary system exhibits higher total stacking density and face-on stacking numbers compared to the binary counterpart. This enhanced molecular packing creates more transport pathways for charge carriers, ultimately contributing to the observed highest PCE.

Nanoscale morphological characteristics of the blend films were comprehensively studied using atomic force microscopy-based infrared (AFM-IR). All three blend films exhibited continuous fibrillar networks, accompanied by uniform and smooth surfaces as evidenced by the root-mean-square (RMS) roughness values of 1.43 nm for PM6:QD-2, 1.56 nm for PM6:QD-3, and 1.32 nm for PM6:QD-2:BO-4Cl (Figure S21, Supporting Information). AFM-IR signals from the blend films were recorded by detecting the characteristic absorption peak (2216 cm^{-1}) of the C≡N bond in acceptors. As shown in Figure 5b, the PM6:QD-3 blend film displayed significantly larger phase separation between the donor and acceptor compared to both the PM6:QD-2 binary and ternary blend films. The reduced donor-acceptor interfacial contact hindered exciton dissociation and charge transport, resulting in lower J_{SC} and FF in PM6:QD-3. The statistical analysis of nanofiber sizes indicated that PM6:QD-3 had a larger fiber size of 21.5 nm than PM6:QD-2 (20.1 nm) and PM6:QD-2:BO-4Cl (20.3 nm) (Figure S22, Supporting Information). Excessive crystallization leads to the unfavorable morphology of PM6:QD-3, impairing charge transport. Furthermore, the addition of BO-4Cl can increase the crystallinity which facilitates promote carrier transport.

The degree of donor/acceptor (D/A) phase separation is strongly influenced by their miscibility. We quantified this relationship by calculating the Flory-Huggins interaction parameter (χ) from contact angle measurements (Figure S23, Supporting Information), where a lower χ value indicates higher miscibility. Compared with PM6:QD-3 (χ = 0.41), PM6:QD-2 exhibited a significantly smaller χ value of 0.22 (Table S10, Supporting Information). These results demonstrate that the higher miscibility between PM6 and QD-2 likely promotes more moderate D/A phase separation, as confirmed by both AFM-IR and electrostatic potential analyses.

The molecular orientation and crystallinity of different blend films were characterized by GIWAXS (Figure 5c,d; Table S11, Supporting Information). All acceptor-based films exhibited a preferential face-on orientation, as evidenced by distinct (010) π–π stacking diffraction peaks in the out-of-plane (OOP) direction and (100) lamellar stacking diffraction peaks in the in-plane (IP) direction. This preferred orientation facilitates vertical charge transport. Notably, the PM6:QD-3 blend film showed a reduced diffraction peak intensity at 0.23 $Å^{-1}$ compared to the pristine acceptor film, suggesting suppressed molecular disorder upon blending with PM6.

Furthermore, in the out-of-plane (OOP) direction, all three systems exhibited more compact π–π stacking distances of 3.65 Å. Although the PM6:QD-3 blend film showed stronger crystallization (with a higher coherence length (CCL) of 19.23 Å) compared to PM6:QD-2 (CCL = 14.10 Å), its imperfect face-on orientation still hindered the overall charge transport capability, resulting in inferior device performance relative to the PM6:QD-2-based device. The addition of BO-4Cl enhanced the crystallinity

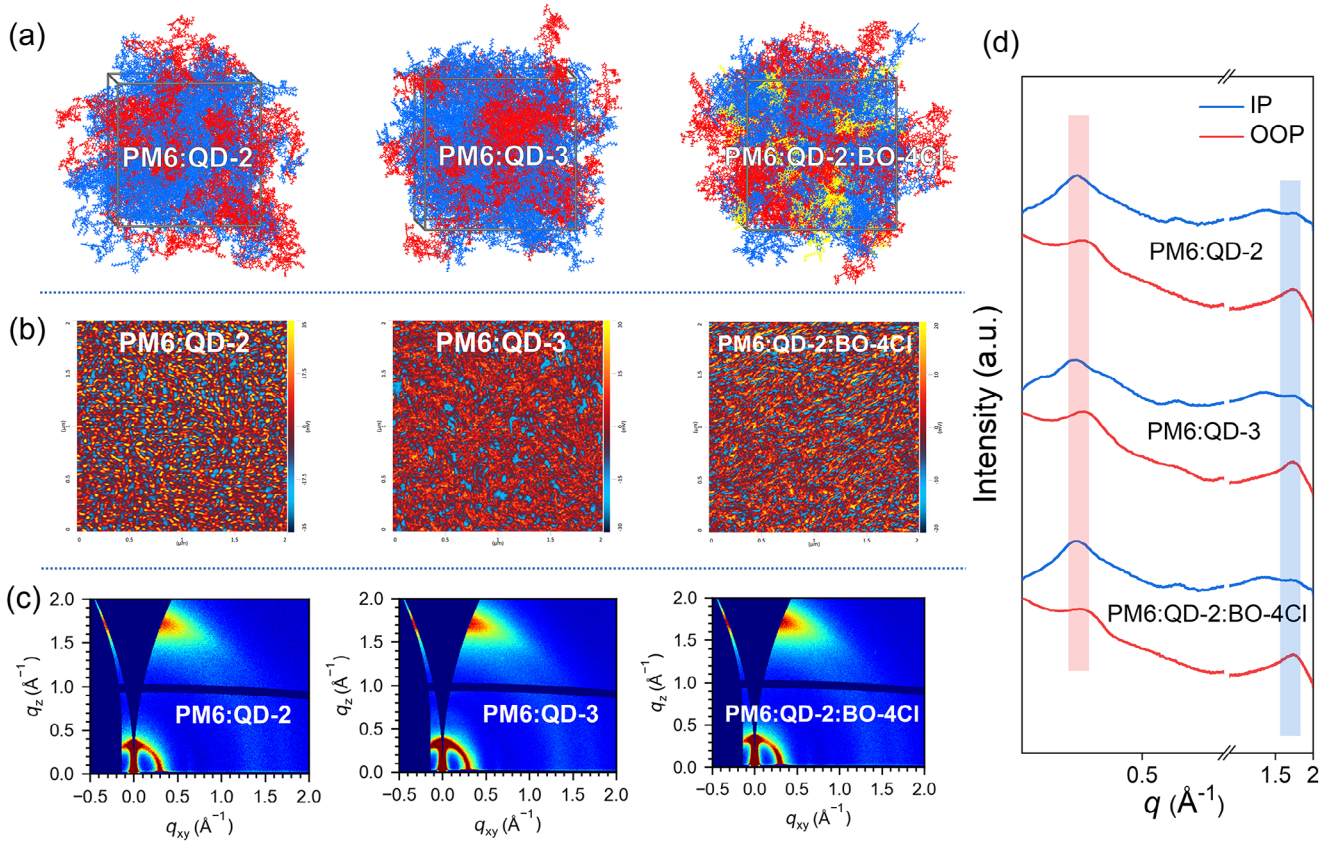

Figure 5. a) MD simulation of the structure of PM6:QD-2, PM6:QD-3, and PM6:QD-2:BO-4Cl, where the red, blue, and yellow colors correspond to PM6, QD-2/QD-3 and BO-4Cl, respectively. b) AFM-IR phase images of three blended films by measuring the 2216 cm^{-1} signal of acceptors, in which donor and acceptor domains were marked with blue and red colors, respectively. c) 2D GIWAXS patterns of blended films. d) Extracted line-cut profiles from 2D GIWAXS patterns of blended films.

of the PM6:QD-2 film in both OOP and in-plane (IP) directions. The improved crystallinity reduces charge recombination and promoted carrier transport, leading to higher PCE in the ternary system.

3. Conclusion

This work demonstrates the profound impact of synergistic control between molecular topology and linker units in advancing dimer acceptors for high-performance OSCs. Through innovative head-to-tail coupling, we developed QD-2 (vinylene-bridged) and QD-3 (ethynylene-bridged) dimers that exhibit distinct structure-property relationships governed by their respective linkers. The vinylene-bridged QD-2 shows particularly remarkable performance, achieving superior PCEs of 19.39% (binary) and 20.04% (ternary), significantly outperforming the PCE of PM6:QD-3 (18.08%). Comprehensive characterization reveals that the advantages of QD-2 stem from multiple synergistic factors: reduced energy disorder, suppressed electron-phonon coupling, and favorable fibrous morphology, all of which collectively enhance exciton dissociation and charge transport dynamics. Through combined spectroscopic, computational, and morphological analyses, this work demonstrates that vinylene-bridged QD-2 achieves an optimal balance between molecular order and interfacial mixing, enabling efficient charge generation and transport. Importantly, both dimer acceptors maintain excellent thermal stability due to their high Tg values, addressing a critical challenge in OSCs. This work opens promising avenues for developing stable, high-efficiency organic photovoltaics through novel topological structure design strategies.

Supporting Information

Supporting Information is available from the Wiley Online Library or from the author.

Acknowledgements

The authors gratefully acknowledge the financial support from the National Natural Science Foundation of China (52025033, 52373189, and 22361132530), Ministry of Science and Technology of China (2022YFB4200400).

Conflict of Interest

The authors declare no conflict of interest.

Data Availability Statement

The data that support the findings of this study are available from the corresponding author upon reasonable request.

Keywords

dimer acceptors, head-to-tail, high efficiency, high stability, organic solar cells

Received: September 1, 2025
Revised: October 27, 2025
Published online:

[1] S. Guan, Y. Li, C. Xu, N. Yin, C. Xu, C. Wang, M. Wang, Y. Xu, Q. Chen, D. Wang, L. Zuo, H. Chen, *Adv. Mater.* **2024**, *36*, 2400342.
[2] L. Zhu, M. Zhang, G. Zhou, Z. Wang, W. Zhong, J. Zhuang, Z. Zhou, X. Gao, L. Kan, B. Hao, F. Han, R. Zeng, X. Xue, S. Xu, H. Jing, B. Xiao, H. Zhu, Y. Zhang, F. Liu, *Joule* **2024**, *8*, 3153.
[3] Y. Jiang, S. Sun, R. Xu, F. Liu, X. Miao, G. Ran, K. Liu, Y. Yi, W. Zhang, X. Zhu, *Nat. Energy* **2024**, *9*, 975.
[4] H. Chen, Y. Huang, R. Zhang, H. Mou, J. Ding, J. Zhou, Z. Wang, H. Li, W. Chen, J. Zhu, Q. Cheng, H. Gu, X. Wu, T. Zhang, Y. Wang, H. Zhu, Z. Xie, F. Gao, Y. Li, Y. Li, *Nat. Mater.* **2025**, *24*, 444.
[5] C. Li, J. Song, H. Lai, H. Zhang, R. Zhou, J. Xu, H. Huang, L. Liu, J. Gao, Y. Li, M. H. Jee, Z. Zheng, S. Liu, J. Yan, X.-K. Chen, Z. Tang, C. Zhang, H. Y. Woo, F. He, F. Gao, H. Yan, Y. Sun, *Nat. Mater.* **2025**, *24*, 433.
[6] X. Gu, Y. Wei, R. Zeng, J. Lv, Y. Hou, N. Yu, S. Tan, Z. Wang, C. Li, Z. Tang, Q. Peng, F. Liu, Y. Cai, X. Zhang, H. Huang, *Angew. Chem., Int. Ed.* **2025**, *64*, 202418926.
[7] J. Yuan, Y. Zhang, L. Zhou, G. Zhang, H.-L. Yip, T.-K. Lau, X. Lu, C. Zhu, H. Peng, P. A. Johnson, M. Leclerc, Y. Cao, J. Ulanski, Y. Li, Y. Zou, *Joule* **2019**, *3*, 1140.
[8] C. Li, J. Zhou, J. Song, J. Xu, H. Zhang, X. Zhang, J. Guo, L. Zhu, D. Wei, G. Han, J. Min, Y. Zhang, Z. Xie, Y. Yi, H. Yan, F. Gao, F. Liu, Y. Sun, *Nat. Energy* **2021**, *6*, 605.
[9] Y. Cui, H. Yao, J. Zhang, K. Xian, T. Zhang, L. Hong, Y. Wang, Y. Xu, K. Ma, C. An, C. He, Z. Wei, F. Gao, J. Hou, *Adv. Mater.* **2020**, *32*, 1908205.
[10] Y. Shi, Y. Chang, K. Lu, Z. Chen, J. Zhang, Y. Yan, D. Qiu, Y. Liu, M. A. Adil, W. Ma, X. Hao, L. Zhu, Z. Wei, *Nat. Commun.* **2022**, *13*, 3256.
[11] H. Chen, Y. Zou, H. Liang, T. He, X. Xu, Y. Zhang, Z. Ma, J. Wang, M. Zhang, Q. Li, C. Li, G. Long, X. Wan, Z. Yao, Y. Chen, *Sci. China Chem.* **2022**, *65*, 1362.
[12] Y. Jiang, Y. Li, F. Liu, W. Wang, W. Su, W. Liu, S. Liu, W. Zhang, J. Hou, S. Xu, Y. Yi, X. Zhu, *Nat. Commun.* **2023**, *14*, 5079.
[13] Y. Qin, N. Balar, Z. Peng, A. Gadisa, I. Angunawela, A. Bagui, S. Kashani, J. Hou, H. Ade, *Joule* **2021**, *5*, 2129.
[14] J.-W. Lee, C. Sun, D. J. Kim, M. Y. Ha, D. Han, J. S. Park, C. Wang, W. B. Lee, S.-K. Kwon, T.-S. Kim, Y.-H. Kim, B. J. Kim, *ACS Nano* **2021**, *15*, 19970.
[15] H. Zhuo, X. Li, J. Zhang, C. Zhu, H. He, K. Ding, J. Li, L. Meng, H. Ade, Y. Li, *Nat. Commun.* **2023**, *14*, 7996.
[16] N. Liang, D. Meng, Z. Wang, *Acc. Chem. Res.* **2021**, *54*, 961.
[17] X. Gu, X. Zhang, H. Huang, *Angew. Chem., Int. Ed.* **2023**, *62*, 202308496.
[18] H. Wang, C. Cao, H. Chen, H. Lai, C. Ke, Y. Zhu, H. Li, F. He, *Angew. Chem. Int. Ed.* **2022**, *61*, 202201844.
[19] F. Qi, Y. Li, R. Zhang, F. R. Lin, K. Liu, Q. Fan, A. K. Y. Jen, *Angew. Chem. Int. Ed.* **2023**, *62*, 202303066.
[20] M. Lv, Q. Wang, J. Zhang, Y. Wang, Z. G. Zhang, T. Wang, H. Zhang, K. Lu, Z. Wei, D. Deng, *Adv. Mater.* **2023**, *36*, 2310046.
[21] J. Wan, T. Wang, R. Sun, X. Wu, S. Wang, M. Zhang, J. Min, *Adv. Mater.* **2023**, *35*, 2302592.
[22] H. Chen, Z. Zhang, P. Wang, Y. Zhang, K. Ma, Y. Lin, T. Duan, T. He, Z. Ma, G. Long, C. Li, B. Kan, Z. Yao, X. Wan, Y. Chen, *Energy Environ. Sci.* **2023**, *16*, 1773.
[23] S. Oh, D. Jeong, K. Bae, G. U. Kim, T. N. L. Phan, J. W. Lee, J. Park, D. Lee, S. Cho, B. J. Kim, *Adv. Funct. Mater.* **2024**, *34*, 2406501.
[24] S. Li, R. Zhang, M. Zhang, J. Yao, Z. Peng, Q. Chen, C. Zhang, B. Chang, Y. Bai, H. Fu, Y. Ouyang, C. Zhang, J. A. Steele, T. Alshahrani, M. B. J. Roeffaers, E. Solano, L. Meng, F. Gao, Y. Li, Z.-G. Zhang, *Adv. Mater.* **2023**, *35*, 2206563.
[25] Y. Ding, W. A. Memon, S. Xiong, S. Gong, M. Li, Z. Deng, H. Liu, Y. Liu, X. Chen, N. Zheng, F. He, *Adv. Mater.* **2025**, *37*, 2501671.
[26] K. Ma, H. Liang, Y. Wang, T. He, T. Duan, X. Si, W. Shi, G. Long, X. Cao, Z. Yao, X. Wan, C. Li, B. Kan, Y. Chen, *Sci. China Chem.* **2024**, *67*, 1687.
[27] H. Liu, L. Tang, T. Li, F. Yi, W. Su, K. Xiang, B. Dong, Z. Yao, K. Wang, T. Hu, Z. Bi, H. Bai, J. Chen, X. Wang, Y. Liu, R. Ma, M. Xiao, W. Ma, Q. Fan, *Angew. Chem. Int. Ed.* **2025**, *64*, 202503721.
[28] Y. Ding, W. A. Memon, D. Zhang, Y. Zhu, S. Xiong, Z. Wang, J. Liu, H. Li, H. Lai, M. Shao, F. He, *Angew. Chem. Int. Ed.* **2024**, *63*, 202403139.
[29] M. Zhang, Z. Wang, L. Zhu, R. Zeng, X. Xue, S. Liu, J. Yan, Z. Yang, W. Zhong, G. Zhou, L. Kan, J. Xu, A. Zhang, J. Deng, Z. Zhou, J. Song, H. Jing, S. Xu, Y. Zhang, F. Liu, *Adv. Mater.* **2024**, *36*, 2407297.
[30] W. Shi, Q. Han, W. Zhao, R. Wang, L. Li, G. Song, X. Chen, G. Long, Z. Yao, Y. Lu, C. Li, X. Wan, Y. Chen, *Energy Environ. Sci.* **2025**, *18*, 5356.
[31] J.-W. Lee, C. Sun, C. Lee, Z. Tan, T. N.-L. Phan, H. Jeon, D. Jeong, S.-K. Kwon, Y.-H. Kim, B. J. Kim, *ACS Energy Lett.* **2023**, *8*, 1344.
[32] C. Sun, J.-W. Lee, Z. Tan, T. N.-L. Phan, D. Han, H.-G. Lee, S. Lee, S.-K. Kwon, B. J. Kim, Y.-H. Kim, *Adv. Energy Mater.* **2023**, *13*, 2301283.
[33] M. de Jong, L. Seijo, A. Meijerink, F. T. Rabouw, *Phys. Chem. Chem. Phys.* **2015**, *17*, 16959.
[34] T. D. Krauss, F. W. Wise, *Phys. Rev. B* **1997**, *55*, 9860.
[35] V. Coropceanu, M. Malagoli, D. A. da Silva Filho, N. E. Gruhn, T. G. Bill, J. L. Brédas, *Phys. Rev. Lett.* **2002**, *89*, 275503.
[36] D. Liu, J. Mun, G. Chen, N. J. Schuster, W. Wang, Y. Zheng, S. Nikzad, J.-C. Lai, Y. Wu, D. Zhong, Y. Lin, Y. Lei, Y. Chen, S. Gam, J. W. Chung, Y. Yun, J. B. H. Tok, Z. Bao, *J. Am. Chem. Soc.* **2021**, *143*, 11679.
[37] X. Cao, J. Guo, Z. Li, X. Bi, H. Liang, Z. Xiao, Y. Guo, X. Jia, Z. Xu, K. Ma, Z. Yao, B. Kan, X. Wan, C. Li, Y. Chen, *ACS Energy Lett.* **2023**, *8*, 3494.
[38] J. Ding, H. Mou, H. Chen, J. Xu, W. Sun, J. Zhu, Y. Wang, Y. Huang, Y. Li, Y. Li, *Adv. Mater.* **2025**, *37*, 2420439.
[39] Z. Zhang, Y. Li, G. Cai, Y. Zhang, X. Lu, Y. Lin, *J. Am. Chem. Soc.* **2020**, *142*, 18741.
[40] C. Sun, J.-W. Lee, C. Lee, D. Lee, S. Cho, S.-K. Kwon, B. J. Kim, Y.-H. Kim, *Joule* **2023**, *7*, 416.
[41] L. Zhu, M. Zhang, J. Xu, C. Li, J. Yan, G. Zhou, W. Zhong, T. Hao, J. Song, X. Xue, Z. Zhou, R. Zeng, H. Zhu, C.-C. Chen, R. C. I. MacKenzie, Y. Zou, J. Nelson, Y. Zhang, Y. Sun, F. Liu, *Nat. Mater.* **2022**, *21*, 656.
[42] W. Zhao, A. Li, Y. Zhou, Z. Hao, J. Yang, T. Yan, X. Wan, X. Chen, Y. Chen, G. Long, *ACS Appl. Mater. Interfaces* **2025**, *17*, 45947.
[43] J. Wang, P. Wang, T. Chen, W. Zhao, J. Wang, B. Lan, W. Feng, H. Liu, Y. Liu, X. Wan, G. Long, B. Kan, Y. Chen, *Angew. Chem., Int. Ed.* **2025**, *64*, 202423562.

